

# Flexible Fibers in Turbulence

Cristian Marchioli,<sup>1</sup> Marco Edoardo Rosti,<sup>2</sup>  
and Gautier Verhille<sup>3</sup>

<sup>1</sup>Department of Engineering and Architecture, University of Udine, Udine, Italy;  
email: marchioli@uniud.it

<sup>2</sup>Complex Fluids and Flows Unit, Okinawa Institute of Science and Technology Graduate  
University, Okinawa, Japan; email: marco.rosti@oist.jp

<sup>3</sup>Aix Marseille Université, CNRS, Centrale Méditerranée, IRPHE, Marseille, France;  
email: gautier.verhille@cnrs.fr

Annu. Rev. Fluid Mech. 2026. 58:167–92

First published as a Review in Advance on  
September 22, 2025

The *Annual Review of Fluid Mechanics* is online at  
fluid.annualreviews.org

<https://doi.org/10.1146/annurev-fluid-112723-050451>

Copyright © 2026 by the author(s). This work is licensed under a Creative Commons Attribution 4.0 International License, which permits unrestricted use, distribution, and reproduction in any medium, provided the original author and source are credited. See credit lines of images or other third-party material in this article for license information.



**ANNUAL  
REVIEWS CONNECT**

[www.annualreviews.org](http://www.annualreviews.org)

- Download figures
- Navigate cited references
- Keyword search
- Explore related articles
- Share via email or social media

## Keywords

turbulence, fibers, flexibility

## Abstract

In this article, we review recent progress in the fundamental understanding of the motion of flexible fibers in a turbulent flow, made through multiscale experiments and simulations. Emphasis is given to problems involving flexible fibers that can be conveniently described with discrete and continuum models closely related to the slender body theory. Current state-of-the-art measurement and simulation methods, including optical techniques, Euler–Lagrange approaches for tracking large swarms of fibers, and recent methodologies for simulating finite-size fibers, are discussed. The capabilities of simulations and experiments are surveyed in connection with the current physical understanding of how flexible fibers interact with the full spectrum of length scales and timescales of turbulence. We review the phenomenological and statistical features of fiber dispersion and spatial distribution. We also discuss the relevant aspects of fiber rotation and deformation, highlighting their connection with mechanisms such as fragmentation and turbulence modulation, which are known to exhibit peculiar features in the case of flexible fibers. We conclude our analysis by providing an outlook on future research direction paths, open methodological issues, and expected advances, in particular those associated with the study of flexible particles in a broader sense.

## 1. INTRODUCTION

Flexible fibers are common in many industrial and natural turbulent flows, where they are characterized by a wide range of sizes (length, aspect ratio), specific density, and flexibility, a property that is typically associated with the Young modulus of the material composing the fiber. Well-known examples are fibers in the pulp and paper industry (Switzer & Klingenberg 2004, Lundell et al. 2011) and microplastics and algae in oceanic environments (du Roure et al. 2019, Bergfreund et al. 2024, Parrella et al. 2024, Sugathapala et al. 2025). More recently, studies of the long-range transport of microplastic fibers in the atmosphere (Bhowmick et al. 2024, Candelier et al. 2024, Tatsii et al. 2024) have appeared in the literature. An innovative application of flexible fibers is related to the use of buckled flexible filaments as vortex generators to enhance heat transfer in heat sink systems and limit the energy consumption of electronic devices (Chen et al. 2024). Flexible fibers are also found in gas–solid fluidization systems loaded with fibrous granular materials (Xu et al. 2023).

Driven by the practical relevance of all these applications, the problem of turbulent flows laden with flexible fibers has attracted growing attention within the multiphase flow community over the last decade. Significant progress in our understanding of these flows has been made, thanks to unprecedented advances in available measurement and simulation techniques (Olivieri et al. 2022b, Giurgiu et al. 2024). This review is motivated by the need to summarize the most recent findings that concern the translation, rotation, and deformation of flexible fibers dispersed in a turbulent flow, highlighting the main phenomenological and statistical features but also surveying the experimental and numerical investigation techniques that are currently adopted. Because the focus is on turbulent flows, this review provides a natural complement to that by du Roure et al. (2019), where the behavior of flexible fibers in viscous flows at low Reynolds numbers was discussed.

The capability of fibers to deform under the action of a turbulent flow, associated with the nonspherical shape of the fibers, increases significantly the number of degrees of freedom and may add much complexity to the interaction that the fibers have with the different scales of motion (which are defined in the sidebar titled Turbulent Scales). This leads to significant departures from the ideal case of spherical particles but also from the case of rigid fibers, which has been nicely addressed in a review by Voth & Soldati (2017). The resulting dynamical behavior, governed by translation, rotation, and deformation, is difficult to reproduce through models and simulations, also due to the complexity of the Navier–Stokes equations as opposed to the relative simplicity of the Stokes equations that can be used at low Reynolds numbers. It is equally challenging to make measurements with suitable space and time resolution, in view of the strong fiber anisotropy. These tasks are particularly demanding for fibers that have a high aspect ratio, which most often exhibit the strongest tendency to deform. In this review, we focus our analysis precisely on this kind of fibers, because of their practical importance: High-aspect-ratio fibers are very common in many industrial and environmental processes, as well as in fundamental research, where they are

### TURBULENT SCALES

The inertial range of turbulence is the region of the turbulent kinetic energy spectrum in which turbulent kinetic energy is purely transferred to smaller scales, where it is eventually dissipated. This region is located between the integral length  $L_I$ , at which the energy is injected into the flow, and the Kolmogorov length  $\eta_K = (v^3/\epsilon)^{1/4}$ , at which energy dissipation occurs. Here,  $\nu = \mu/\rho$  is the fluid kinematic viscosity and  $\epsilon$  is the energy dissipation rate per unit mass. The small-scale dynamics of the flow is characterized by the Kolmogorov time  $\tau_K = (\nu/\epsilon)^{1/2}$ , and the typical lifetime of a vortical structure with size  $\ell$  within the inertial range is  $\tau_\ell = \tau_K(\ell/\eta_K)^{-2/3}$ .

usually employed to run reliable experiments. Considering that fibers occur in a dazzling variety of shapes, we further concentrate our discussion on fibers that have a circular cross section and a constant diameter and are straight at equilibrium.

Although we consider a rather specific type of particle, the body of research is still vast. Therefore, we limit our attention to the case of archetypal turbulent flows (homogeneous turbulence and wall-bounded flows) laden with flexible fibers that are heavier than or at most have the same density as the incompressible Newtonian fluid. This choice is in line with recent reviews that have discussed the behavior of spherical (Brandt & Coletti 2022) and nonspherical (Voth & Soldati 2017) particles in turbulence. We begin by presenting the parameter space, as defined by convenient nondimensional numbers, and the dynamical regimes identified therein. We then continue by discussing the behavior of individual fibers: A proper understanding of this behavior is essential to set the stage for future studies of transport, dispersion, and settling in turbulent suspensions, for which, however, additional physical effects such as intrafiber and interfiber interactions must be considered.

## 2. PARAMETER SPACE AND NONDIMENSIONAL NUMBERS

To understand the relevant parameter space and nondimensional numbers that can be used to characterize a turbulent suspension of flexible fibers, let us start by considering the simplest theoretical framework that can be invoked to characterize their deformations. We assume here that the fibers are made of a Hookean material, so they are purely elastic (meaning they exhibit no viscoelasticity) and obey linear elasticity. These deformations can be described by the Euler–Bernoulli beam theory, in which the conformation of the fiber is characterized by its neutral axis, defined as the axis along which the longitudinal stresses and strains of the deformed fiber are equal to zero in the absence of stretching or compression. For a homogeneous cylindrical fiber, this axis corresponds to the geometric centroid of the cross section. In most cases, the equation used to describe the evolution of the neutral axis is the Euler–Bernoulli equation, the derivation of which can be found in classical textbooks (Landau & Lifshitz 1959, Audoly & Pomeau 2010):

$$\sigma \partial_t^2 \mathbf{X} - \partial_s(T \partial_s \mathbf{X}) + B \partial_s^4 \mathbf{X} = \mathbf{F}. \quad 1.$$

Here,  $s$  is the curvilinear coordinate,  $\mathbf{X}$  denotes the position of a point on the neutral axis, and  $\sigma$  and  $B$  are the linear density and bending modulus of the fiber, respectively. For a cylindrical fiber of length  $l$ , diameter  $d$ , density  $\rho_f$ , and Young modulus  $E$ , one gets  $\sigma = \pi d^2 \rho_f / 4$  and  $B = \pi E d^4 / 64$ . In addition,  $T = \int f_{\parallel} ds + B |\partial_s \mathbf{X}|^2$  is the tension and  $f_{\parallel}$  the parallel component of the linear force applied to the fiber. On the left-hand side of Equation 1, the first term accounts for fiber inertia, the second term corresponds to the contribution of the tangential stress and is related to fiber extensibility, and the third term represents the resistance to bending. The term on the right-hand side corresponds to the perpendicular component of the external forces, including the hydrodynamic ones. In the slender body approximation, the external forces reduce to  $\bar{\eta}(\mathbf{u} - \partial_t \mathbf{X})$ , with  $\bar{\eta}$  the viscosity tensor and  $\mathbf{u} - \partial_t \mathbf{X}$  the slip velocity between the fluid and the fiber. It has to be noticed that Equation 1 neglects the torsion of the fiber, an assumption that is justified thereafter. Equation 1 is complemented with an appropriate set of boundary conditions:  $\partial^3 \mathbf{X} / \partial s^3|_{s=l} = \mathbf{0}$  and  $\partial^2 \mathbf{X} / \partial s^2|_{s=l} = \mathbf{0}$  at the free ends of the fiber, along with  $T|_{s=l} = 0$ . A normal mode analysis of the Euler–Bernoulli equation, in the absence of any external forcing, yields the natural frequency (first mode)  $f_{\text{nat}} \approx 22.3733 / (dl^2) \sqrt{\gamma / (\sigma \pi^3)}$ , which plays a significant role in determining the dynamical response of the filaments.

For fibers, three types of deformation can be defined: bending, stretching, and twisting. The timescales that characterize these deformations depend on the importance of the viscous term

## STOKES NUMBER AND REYNOLDS NUMBER FOR A FIBER

The Stokes number is generally defined as  $St = \tau_f/\tau$ , where  $\tau_f = \rho_f d^2/18\mu$  is the translational relaxation time of the fiber, with  $\rho_f$  the fiber density,  $d$  the fiber cross-sectional diameter, and  $\tau$  the characteristic timescale of the flow. The definition of  $\tau$  depends on the properties of the flow. In homogeneous isotropic turbulence (HIT), a standard approach is to set  $\tau = \tau_K$  for short fibers (with length  $l \simeq \eta_K$ ) and  $\tau = \tau_K(l/\eta_K)^{2/3}$  for long fibers (with  $l \simeq L_I \gg \eta_K$ ). This last relation yields

$$St = \frac{\rho_f}{\rho} \left( \frac{d}{\eta_K} \right)^{4/3} \left( \frac{d}{l} \right)^{2/3}. \quad \text{SB1.}$$

In wall-bounded turbulence, it is customary to set  $\tau = \nu/u_*^2$ , with  $u_*$  the friction (or shear) velocity.

The fiber Reynolds number is generally defined as  $Re_f = |\mathbf{u} - \mathbf{v}|L/\nu$ , where  $\mathbf{u} - \mathbf{v}$  is the fiber slip velocity relative to the fluid and  $L$  is a characteristic dimension of the fiber, e.g.,  $l$  or  $d$ . The calculation of the slip velocity may change depending on the specific fiber model adopted. For example, when the fiber is modeled as a chain of elements (see Section 3.2.1), the slip velocity is calculated for each element in the chain, using the velocities at the center of mass of the element and considering its orientation, as done by Dotto & Marchioli (2019). When the fiber is modeled as a homogeneous inextensible elastic filament (see Section 3.2.2), the difference  $\Delta\mathbf{u}$  between the fiber velocity at its midpoint and the local fluid velocity, averaged within a spherical shell centered on the midpoint, is used, as done by Rosti et al. (2018). This yields  $Re_p = d\sqrt{\langle \Delta\mathbf{u} \cdot \Delta\mathbf{u} \rangle}/\nu$ . The angular brackets  $\langle \rangle$  denote an average over all fibers in the flow.

in Equation 1. If the viscous term is larger than the inertial one, the regime is called overdamped, whereas the regime is called underdamped when the viscous term is negligible. These two regimes can be parameterized by the Stokes number (see the sidebar titled Stokes Number and Reynolds Number for a Fiber). In the overdamped regime (underdamped), namely when  $St \ll 1$  ( $St \gg 1$ ), the typical timescale is the relaxation time (the period of oscillation  $T_o$ ), given by the ratio of the bending term and the viscous (inertial) term in the Euler–Bernoulli equation. In this section, we first focus on the overdamped regime ( $St \ll 1$ ), for which fiber deformations have been characterized extensively.

The characteristic timescale of deformation can be estimated by balancing the elastic term and the viscous damping term in the limit of fluid at rest and linear dissipation (Powers 2010). Note that, in reality, the viscous drag tensor is not strictly isotropic, but only its order of magnitude is needed here to estimate the timescale. For bending, the elastic term  $B\partial_s^4\mathbf{X}$  scales as  $B\delta/l^4$ , with  $\delta$  the amplitude of the deformation, and the viscous term  $\mu\partial_t\mathbf{X}$  scales as  $\mu\delta/\tau_b$ . Thus, the relaxation timescale of bending,  $\tau_b$ , is given by

$$\tau_b \sim \frac{\mu l^4}{B} \sim \frac{\mu l^4}{Ed^4} \quad 2.$$

for a homogeneous cylindrical fiber. The same force balance can be done to estimate the stretching timescale,  $\tau_s$ . For this kind of deformation, the elastic term scales as  $Ed^2\delta/l^2$  and the viscous one as  $\mu\delta/\tau_s$ , thus leading to

$$\tau_s \sim \frac{\mu l^2}{Ed^2}. \quad 3.$$

The characteristic timescale of twisting,  $\tau_t$ , is given by a torque balance rather than a force balance. In this case, the linear viscous torque is  $d\mu\partial_t(d\theta)$ , and the elastic torque is  $C_t\partial_{ss}\theta \sim EC_t\theta/l^2$ , where  $C_t$  is the torsional rigidity, which scales as  $C_t \sim d^4$  for a cylindrical fiber. The twisting timescale is

thus given by

$$\tau_t \sim \frac{d^2 l^2 \mu}{EC_t} \sim \frac{\mu l^2}{Ed^2}. \quad 4.$$

Comparing these three timescales, it can be noticed that the relaxation time of bending is much longer than the relaxation time of both stretching and twisting when the fiber aspect ratio is large ( $l \gg d$ ), since both  $\tau_b/\tau_s$  and  $\tau_b/\tau_t$  scale as  $(l/d)^2 \gg 1$ . For this reason, most studies have focused only on bending, neglecting stretching and twisting, with the fiber inextensibility enforced by the tension term  $T$  in the Euler–Bernoulli equation. In this review, only the bending of inextensible fibers is discussed. This discussion can be extended to the underdamped regime by replacing the relaxation time with the period of oscillation  $T_o$ , obtained by balancing the inertial term  $\sigma \partial_t^2 \mathbf{X}$ , which scales as  $\sigma \delta / T_o^2$ , and the bending elastic term  $B \partial_s^4 \mathbf{X}$ , which still scales as  $B \delta / l^4$ . This balance yields

$$T_o \sim \left( \frac{\sigma l^4}{B} \right)^{1/2} \sim \left( \frac{\sigma l^4}{Ed^4} \right)^{1/2}. \quad 5.$$

Throughout the remainder of this review, the deformations of a fiber are characterized by its deformability, measured by the ratio of its length over a typical elastic length (see the sidebar titled Rigid Versus Flexible), and by the nature of the forcing, which depends on the ratio of the fiber length over the Kolmogorov length. The different regimes typically encountered are sketched in **Figure 1**, together with the range of applicability of currently available experiments and simulations.

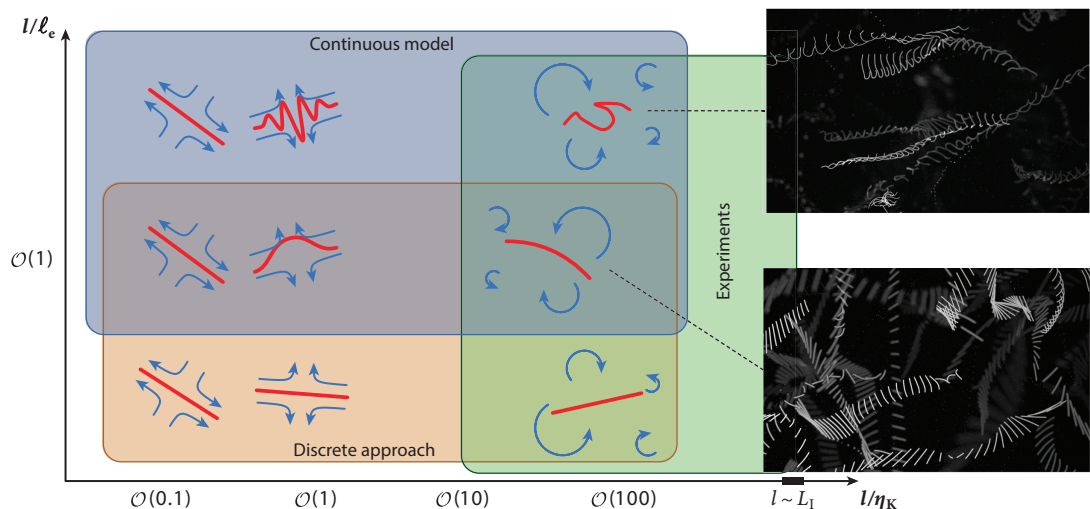


**Figure 1**

Sketch of the different regimes of deformation for a flexible fiber (*thick red lines*), parameterized by the ratio of fiber length  $l$  to the linear elastic length  $\ell_e$ , and the optimal range of applicability of experiments and simulations, based on the ratio of fiber length  $l$  to the Kolmogorov length scale  $\eta_K$ . The shaded areas highlight the complementarity among the different approaches within the parameter space. The upper boundary for  $l$  is represented by the integral length scale of the turbulent flow,  $L_I$ . Short fibers, for which  $l/\eta_K \simeq \mathcal{O}(1)$  or smaller, typically experience a smooth flow. Deformations due to buckling instability are then triggered when the fiber is aligned with the compressive component of the rate-of-strain tensor (*bent blue arrows*). Long fibers, for which  $l/\eta_K \gg \mathcal{O}(1)$  or smaller, experience a multiscale flow and simultaneously interact with many vortices (*half-circle arrows*). In this case, one or several bending modes can be excited, depending on the fiber flexibility.

## RIGID VERSUS FLEXIBLE

The flexibility of a fiber can be quantified using the characteristic length  $\ell_e = B^{1/4}/(\rho\mu\epsilon)^{1/8}$ , which depends on the bending modulus  $B$  of the fiber, on the fluid properties ( $\mu$ ,  $\rho$ ), and on the flow properties, parameterized by  $\epsilon$ . Fibers with a length  $l \gtrsim \ell_e$  are classified as flexible, and fibers with  $l \ll \ell_e$  are classified as rigid. In the following, we refer to  $\ell_e$  as the linear elastic length, since it corresponds to a deformation regime where the nonlinear term in the Euler–Bernoulli equation is negligible.

### 3. METHODOLOGIES

#### 3.1. Experimental Techniques

The fibers used in experiments at high-Reynolds-number flows are produced in a very similar way to those used in laminar flows. Most of the fibers are made of silicone or polydimethylsiloxane (PDMS), for which the linear elasticity approximation is valid over a wide range of deformations (Kim et al. 2011). The Young modulus can vary between few tens of kilopascals to hundreds of megapascals. Currently, two main processes exist to produce fibers: molding and microfluidic processing. With molding, silicone or PDMS is injected into a cylindrical tube and remains until the end of the curing process. The inner diameter and length of the tube determine the final geometry of the fiber, allowing the production of fibers with diameters of approximately 150  $\mu\text{m}$  or larger (Verhille & Bartoli 2016, Marchetti et al. 2018). This process is relatively easy to install but quite time-consuming and cannot be used to produce a large number of fibers. In contrast, microfluidic technology enables the easy production of many elongated objects (Mercader et al. 2010, Nunes et al. 2012), though it is more complicated and expensive to install. The diameter can be less than 100  $\mu\text{m}$  with a length of the order of a few centimeters, a range that typically falls within the inertial scales of turbulence when compared to  $\eta_K$ , which varies between 50 and 500  $\mu\text{m}$  in most experiments. To measure the 3D conformation of a flexible fiber, several synchronized high-speed cameras imaging the same volume with different angles of view are generally used. To perform the 3D reconstruction, a model for the camera is needed to determine the position of a point in space from its projections onto the different images. The most classical one is the pinhole model (Faugeras & Luong 2001), also known as the Tsai model. In this model, the camera is characterized by 11 parameters: 6 extrinsic parameters for the position and orientation of the camera within the lab frame and 5 intrinsic parameters that correspond to the scaling factors converting the unit used in the lab (typically millimeters) to pixels, the coordinates of the pinhole projection onto the image plane, and a skew coefficient (Verhille & Bartoli 2016). These different parameters need to be determined by calibration. Note that this model can be refined to correct the optical distortion and the presence of different interfaces (Belden 2013, Agrawal et al. 2012). Other models have also been used to characterize the camera, but they have not been employed for the reconstruction of flexible fibers (Machicoane et al. 2019, Pujara et al. 2021). From this model and the coordinate of the projection of the fiber onto the images, the 3D coordinates in space are determined either by matching each point along the fiber, as it is classically done in particle tracking (Verhille & Bartoli 2016), or by looking at the convex hull volume of the object, since it corresponds to the shape of the object for a fiber (Masuk et al. 2021, Giurgiu et al. 2023). The set of voxels is then fitted with a spline function or a polynomial function to determine the position of the centerline, as shown schematically in **Figure 2**.

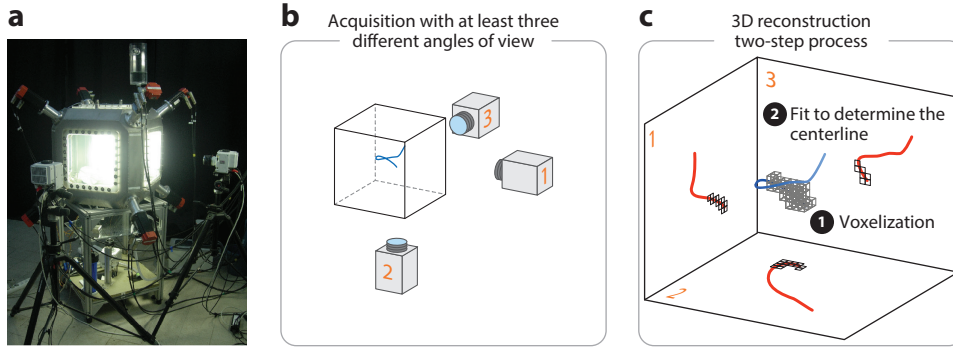


**Figure 2**

Experimental procedure for 3D reconstruction of a flexible fiber. (a) A typical setup for measurements in homogeneous isotropic turbulence must be equipped with at least three synchronized cameras with different angles of view for image acquisition (b). The images so acquired are then used to obtain the shape of the deformed fiber as a set of voxels, knowing the coordinate of the fiber projection on each image and the projection matrices of each camera (c). The set of voxels is then fit using a spline or a polynomial function to determine the position of the centerline.

### 3.2. Numerical Approaches

Numerical approaches to simulating flexible fibers can be divided into discrete approaches and a continuum model, as shown schematically in **Figure 3**. Depending on the way forces and torques are computed, either using models or directly, these approaches can be used to simulate point-wise fibers or fully resolved fibers.

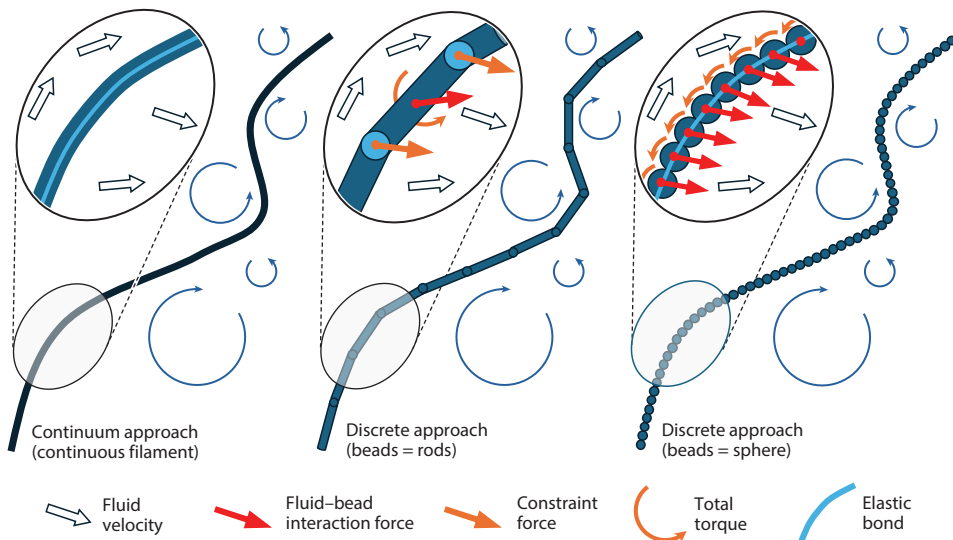


**Figure 3**

Diagram of numerical approaches used to simulate flexible fibers interacting with turbulent vortices. The continuum approach represents fibers as continuous filaments that evolve subject to fluid–structure coupling forces and tensions, while discrete approaches represent fibers as chains of elements (either rods or spheres) that evolve subject to forces, torques, and elastic bonds.

**Slender body theory:** asymptotic technique that can be used to represent the disturbance velocity created by a particle as an integral of Stokeslets distributed along its axis

**3.2.1. Discrete approaches.** The most common class of discrete approaches applies to cases in which  $Re_f$  is small but there is translational and rotational slip between the fiber and the fluid. These methods aim to describe a complex deformable object by the flexible assembly of simple rigid ones, generally composed of discrete elements (spheres or ellipsoids) interacting by some elastic and repulsive forces, but also with the surrounding fluid (Lindström & Uesaka 2007, 2009; Andrić et al. 2013, 2014; Kunhappan et al. 2017; Pei et al. 2018; Dotto & Marchioli 2019). The same type of approach has been used to discretize finite-size fibers (Huang et al. 2007, Wu & Aidun 2010, Favier et al. 2014, Delmotte et al. 2015, Tang et al. 2018) in combination with the immersed boundary method (IBM) (Peskin 1972), exploiting an external boundary force to impose the no-slip boundary condition at the fluid–solid interface, albeit not in turbulence with the exception of Sulaiman et al. (2019). With finite-size fibers, forces and torques are obtained directly from the fluid pressure and stress distributions around the fibers, whereas suitable force and torque models are required for the application to point-wise fibers, as discussed below.

Considering an inertial frame of reference that uses a Cartesian coordinate system with axes  $\{\mathbf{e}_x, \mathbf{e}_y, \mathbf{e}_z\}$ , a generic element in the chain, labeled by subscript  $r$  hereinafter, is associated with a position vector  $\mathbf{X}_r$  and is characterized by density  $\rho_f$ , cross-sectional diameter  $d$ , length  $l_r = \|\mathbf{X}_r - \mathbf{X}_{r+1}\|$ , and aspect ratio  $\Lambda_r = l_r/d$ . For each element, the following dynamical equations of rigid-body motion for translation and rotation hold:

$$m_r \partial_t \mathbf{v}_r = \mathbf{F}_r^H + \mathbf{F}_r^B + \sum_s \mathbf{F}_{r,s}^I + \mathbf{F}_{r+1}^C - \mathbf{F}_r^C, \quad 6.$$

$$\partial_t (\bar{\mathbf{J}}_r \boldsymbol{\omega}_r) = \mathbf{T}_r^H + \sum_s \mathbf{T}_{r,s}^I + \mathbf{T}_{r+1}^b - \mathbf{T}_r^b + l_r \mathbf{X}_r \times (\mathbf{F}_{r+1}^C + \mathbf{F}_r^C). \quad 7.$$

In Equation 6,  $m_r = \rho_f 2\pi \Lambda_r d^3$  is the mass of the element,  $\mathbf{v}_r$  is the translation velocity evaluated at the center of mass of the element, denoted by vector  $\mathbf{p}_r$ ,  $\mathbf{F}_r^H$  is the hydrodynamic drag force exerted by the fluid surrounding the element,  $\mathbf{F}_r^B$  is the body force (e.g., due to gravity),  $\mathbf{F}_{r,s}^I$  is the interaction force due to contact or lubrication that is exerted on element  $r$  by element  $s$  of some other fiber or by a nonadjacent element of the same fiber, and  $\mathbf{F}_{r+1}^C$  and  $\mathbf{F}_r^C$  are the constraint forces produced by element  $r+1$  on element  $r$  and by element  $r$  on element  $r-1$ , respectively. These forces ensure that the endpoints of adjacent elements overlap at all times and are obtained from the following connectivity constraint, which must be added to close the system of equations:  $\mathbf{p}_r + l_r \mathbf{X}_r - (\mathbf{p}_{r+1} - l_{r+1} \mathbf{X}_{r+1}) = \mathbf{0}$ .

In Equation 7,  $\boldsymbol{\omega}_r$  is the angular velocity and  $\bar{\mathbf{J}}_r$  the inertia tensor of the element, which is typically computed as a function of its orientation. The first term on the right-hand side represents the hydrodynamic torque,  $\mathbf{T}_r^H$ , which can be split into a contribution due to the relative spin between the fiber and the surrounding fluid plus a contribution due to the action of the local fluid velocity gradients, respectively. The second term,  $\mathbf{T}_{r,s}^I$ , is the torque due to the interaction force  $\mathbf{F}_{r,s}^I$ . The two terms  $\mathbf{T}_{r+1}^b$  and  $\mathbf{T}_r^b$  represent the bending torque (a similar term can be added in case the twisting torque is considered), while the last term,  $l_r \mathbf{X}_r \times (\mathbf{F}_{r+1}^C + \mathbf{F}_r^C)$ , is the torque contribution of the constraint forces.

The expressions used to compute forces and torques can be selected based on the element's Reynolds number,  $Re_{f,r}$ . Analytical solutions derived for an isolated axisymmetric ellipsoid can be used when  $Re_{f,r} = 0$  (Kim & Karrila 1991) and extended to rod-like elements (Cox 1971). When  $Re_{f,r} > 0$ , inertial effects must be incorporated (Di Giusto et al. 2024), using, for instance, a suitably defined drag coefficient in the expression of  $\mathbf{F}_r^D$  (Dotto & Marchioli 2019). For highly elongated fibers, other approaches are possible, namely the slender body theory (Batchelor 1970,

Cox 1970), which can be used to obtain analytical approximations to the Stokes flow solution for fibers with large aspect ratios (Andersson et al. 2021, Candelier et al. 2024), or the resistive force theory (Kamal & Lauga 2023), which can be used to obtain the translation of any rigid slender body through a viscous fluid, provided that the radius of curvature is large compared with the body radius. The reader is referred to du Roure et al. (2019) for a complete description of these approaches.

**3.2.2. Continuum model.** An alternative approach is to model each fiber as a homogeneous, elastic filament that evolves according to a modified Equation 1 in a Lagrangian framework, under the assumption of fiber inextensibility:

$$\partial_s \mathbf{X} \cdot \partial_t \mathbf{X} = 1. \quad 8.$$

Equations 1 and 8 are an extended version of the distributed-Lagrange-multiplier/fictitious-domain formulation of the continuum equations introduced by Yu (2005). In this approach, the tension  $T$  is used to enforce fiber inextensibility, and two terms need to be included in the force  $\mathbf{F}$  on the right-hand-side of Equation 1: the fluid–structure coupling term (see the sidebar titled Backreaction to the Flow) and the fluid acceleration  $\rho \partial_t \dot{\mathbf{X}}$ , used to cancel fluid inertia in the fictitious domain inside the fiber (Yu 2005). When dealing with multiple objects, filament-to-filament

## BACKREACTION TO THE FLOW

When the suspension of fibers is nondilute, their backreaction to the flow must be accounted for. Mutual interactions between the fiber and the fluid are typically enforced via singular force distributions acting on each phase, often implemented in the setting of IBM for fully resolved fibers (Huang et al. 2007, Pinelli et al. 2010, Banaei et al. 2020b, Olivieri et al. 2020, Agrawal et al. 2024). To do so, the equation of motion for the carrier flow, governed by the incompressible Navier–Stokes equations for a Newtonian fluid, is extended by including an additional force  $\mathbf{f}_{\text{fs}}(\mathbf{x}, t)$  that mimics the presence of the solid phase. An equal and opposite force  $\mathbf{F}$  must be present in the equation of motion for the fibers (Equation 1) to enforce the no-slip condition at their surface. This force can be computed as follows: The material points of the immersed fiber are forced to move with the fluid velocity at those points through a no-slip condition  $\dot{\mathbf{X}} = \mathbf{u}(\mathbf{X}, t)$ , with  $\mathbf{X} = \mathbf{X}(s, t)$  the material point position and  $\mathbf{u} = \mathbf{u}(\mathbf{x}, t)$  the fluid velocity. The fluid velocity at the position of the fiber Lagrangian point,  $\mathbf{U} = \mathbf{u}(\mathbf{X}(s, t), t)$ , is obtained by interpolating the fluid velocity at the Eulerian nodes surrounding the Lagrangian point as

$$\mathbf{U}(\mathbf{X}(s, t), t) = \int \mathbf{u}(\mathbf{x}, t) \delta(\mathbf{x} - \mathbf{X}(s, t)) d^3 \mathbf{x}, \quad \text{SB2.}$$

where the  $\delta$  is the Dirac delta function. Using  $\mathbf{U}$ , the fluid–structure forcing term can be obtained as  $\mathbf{F}(s, t) = \kappa(\mathbf{U} - \dot{\mathbf{X}})$ , where  $\kappa$  is a large negative constant (Goldstein et al. 1993, Olivieri et al. 2020). Finally, the forcing on the fluid from the fiber is calculated as

$$\mathbf{f}_{\text{fb}}(\mathbf{x}, t) = \frac{1}{\rho} \int_s \mathbf{F}(s, t) \delta(\mathbf{x} - \mathbf{X}(s, t)) ds. \quad \text{SB3.}$$

The coupling between the fluid and the fiber surface is attained, spreading the force distribution computed by means of a Lagrangian IBM over the Eulerian grid points, enforcing the no-slip condition at the Lagrangian points representing the filaments. The interface between the fluid and the fiber is therefore not sharply captured but diffused among the grid points by means of a window function. Based on this, one can estimate an effective filament diameter of approximately three grid points, namely,  $d = 3 \Delta x$  in units of the Eulerian grid spacing. An improved coupling algorithm to properly enforce the fiber diameter was presented by Pinelli et al. (2010), a method that also allows for a larger order of accuracy.

---

**Inertial subrange:**

region of the turbulent kinetic energy spectrum in which turbulent kinetic energy is purely transferred to smaller scales, where it is dissipated

**Viscous (or dissipation) subrange:**

region of the turbulent kinetic energy spectrum in which molecular viscosity becomes important and viscous dissipation of kinetic energy takes place

**Rate-of-strain tensor:**

describes how a material deforms over time; its eigenvectors represent the directions of maximum and minimum stretching or compression, and the corresponding eigenvalues indicate the rate of deformation in those directions

---

and filament-to-wall collisions must be accounted for as well. However, extensive testing of elastic and inelastic collision models has shown that, from a dynamical standpoint, filament-to-filament collisions are statistically irrelevant in dilute conditions and are therefore often neglected, while filament-to-wall collisions become marginally relevant only for highly flexible fibers (Olivieri et al. 2022b). Thus, it is often enough to account for them using a simple inelastic collision model, in which a repulsive force is applied to the filament points approaching the wall within a range of four grid points. This model is usually called the minimal collision model (Snook et al. 2012). With the exception of the bending factor, which can be handled implicitly to permit larger time steps (Banaei et al. 2020b), the governing equations of motion can be solved using a two-step procedure (Huang et al. 2007): (a) solve a Poisson equation for the tension, obtained by combining Equations 1 and 8 (for more details, see Banaei et al. 2020b), and (b) solve Equation 1 to obtain the revised position of the Lagrangian points defining the filament. After discretizing each fiber with  $N$  evenly spaced Lagrangian points (resulting in a spatial resolution that roughly corresponds to the Eulerian grid spacing), a second-order finite-difference technique on a staggered grid for tension and position can be used to discretize the equations of motion (Huang et al. 2007, Banaei et al. 2020b, Olivieri et al. 2020). Recently, Agrawal et al. (2024) proposed a new framework to capture the large deformation dynamics of fibers. Using a geometrically exact, nonlinear Euler–Bernoulli rod formulation, they showed that even a coarse mesh can deliver accurate results, leading to a major gain in computational efficiency.

## 4. FIBER DEFORMATION

Elongated fibers transported by a turbulent flow may experience fluid velocity changes along their length. This is particularly true for fibers with lengths within the inertial subrange of turbulence, referred to as long fibers hereinafter, for which the velocity variation is nonlinear and the forcing is multiscale. These fibers are expected to behave differently from those with lengths of the order of the Kolmogorov length or smaller, referred to as short fibers hereinafter, which are in the viscous subrange of turbulence. Flexibility represents an additional source of bias in determining the macroscopic outcome of fiber–turbulence interaction, e.g., in terms of overall fiber deformation, motion, and spatial distribution within the flow. In this section, we review fiber deformation by highlighting the different deformation regimes and their statistical characterization.

### 4.1. Deformations of Short Fibers

Deformation statistics generally depends on fiber flexibility but also on the ratio between the particle length and the Kolmogorov length. However, as small elongated objects tend to align preferentially with the extensional direction of the rate-of-strain tensor (Voth & Soldati 2017), short fibers remain straight for most of the time because they experience smooth velocity gradients as they are brought about by the flow. Still, buckling instabilities can be triggered when the fiber is aligned with the compressive direction of the rate-of-strain tensor. Allende et al. (2018) showed that the selected mode of buckling and the probability of its occurrence  $\mathcal{P}_{\text{buck}}$  are governed by the ratio

$$\mathcal{F} = \frac{8\pi\mu l^4}{cB\tau_{\kappa}}, \quad 9.$$

where  $c = -(1 - 2\log \Lambda) \gg 1$ . The probability distribution of buckling events follows an exponential law of the type  $\mathcal{P}_{\text{buck}} \propto \exp[A(\mathcal{F}/\mathcal{F}^*)^{1/2}]$ , which is linked to the probability distribution of the velocity gradients in turbulence.

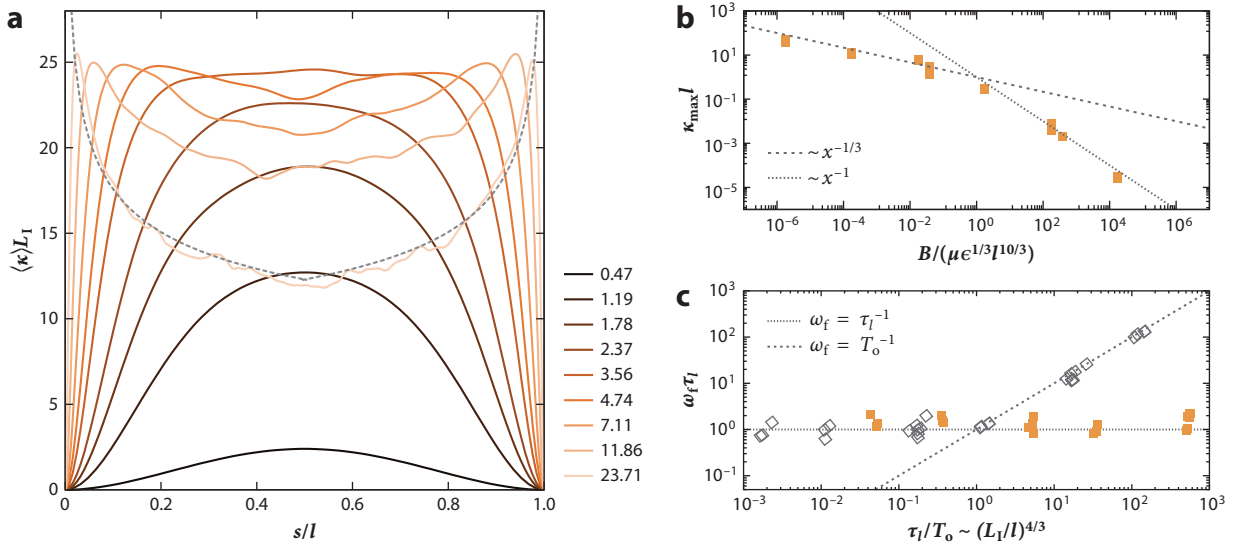


**Figure 4**

(a) Evolution of the mean curvature, as a function of the normalized curvilinear coordinate,  $s/l$ , at varying fiber lengths. The fiber length increases from darker to lighter orange. The dashed line corresponds to the  $s^{-2/9}$  scaling (see Equation 13). (b) Evolution of the mean maximal curvature in the overdamped regime ( $St \ll 1$ ) as a function of the ratio  $(L_v/l)^{10/3}$ . (c) Evolution of the timescale of deformation as a function of the ratio between the forcing timescale,  $\tau_f$ , and the period of oscillation,  $T_o$ . The filled symbols correspond to fibers in the overdamped regime ( $St \ll 1$ ) and the empty symbols to the underdamped regime ( $St \gg 1$ ). Panel *a* adapted with permission from Gay et al. (2018). Panel *b* adapted from Olivieri et al. (2022a) (CC BY 4.0). Panel *c* adapted from Cannon et al. (2024) (CC BY 4.0).

## 4.2. Deformations of Long Fibers

The system is richer for long fibers as they experience nonuniform forcing. In this case, two deformation regimes have been identified (Gay et al. 2018; Rosti et al. 2018, 2020; Olivieri et al. 2022b): The first regime corresponds to moderately flexible fibers and only the first bending mode is excited, while the second corresponds to large deformations associated with fully 3D conformation. These regimes are discussed next with reference to **Figure 4**.

**4.2.1. Weakly flexible fibers: planar conformation.** In the underdamped regime, the deformation timescale, defined as the main frequency of the Fourier transform of the end-to-end distance (Rosti et al. 2018), corresponds to the frequency of the first mode of vibration. In contrast, there is no temporal signature of this bending mode in the overdamped regime, as viscous dissipation prevents oscillations. The main frequency in the overdamped regime corresponds to the typical timescale of the turbulent eddies of size  $l$ :  $\omega_l = l/u_l \sim (l/\eta_K)^{2/3} \tau_K^{-1}$  (see **Figure 4c**) (Olivieri et al. 2021, 2022b). In both regimes, the average conformation is a U shape similar to the first bending mode with maximum curvature at the center of the fiber,  $s = l/2$ , and zero curvature at the extremities,  $s = 0$  and  $s = l$ , due to the boundary condition (see **Figure 4a**) (Gay et al. 2018). Brouzet et al. (2014) proposed an analogy between the deformation of flexible fibers in turbulence and that of semiflexible polymers distorted by thermal fluctuation (Doi & Edwards 1986). Indeed, as for semiflexible polymers (or worm-like polymer chains), the end-to-end distance is governed by the ratio of the fiber length  $l$  over a typical length that is called persistence length,  $\ell_p$ , in polymer theory (Yamakawa 1971) and is equivalent to the linear elastic length  $\ell_e$  introduced in Section 2. However, if  $\ell_p$  can be interpreted as a balance between the thermal energy and the elastic energy stored inside the polymer, this is not the case for  $\ell_e$ , for which the balance of energy

must be replaced by a balance of power. Indeed, in a stationary flow regime, the energy  $\mathcal{E}$  of the system composed of the fibers is on average constant and its rate of change over time must obey the condition

$$\partial_t \mathcal{E} = \mathcal{P}_{\text{inj}} - \mathcal{P}_{\text{dis}} = 0, \quad 10.$$

where  $\mathcal{P}_{\text{inj}}$  and  $\mathcal{P}_{\text{dis}}$  are the power received (given) by the system from (to) turbulence. The power injected by turbulence is proportional to the ratio of the energy contained in an eddy of size  $l$  over the lifetime of the structure:  $\tau_l = l/u_l$ . The dissipated power is proportional to the ratio of the elastic energy stored inside the fiber, which can be expressed as  $\int B\kappa^2(s)ds$  over the lifetime of the deformation, given by the bending relaxation time in the overdamped regime and the first bending mode frequency in the underdamped regime (Verhille 2022). Defining the linear elastic length  $\ell_e$  as the length for which  $\int \kappa^2(s)ds = 1/\ell_e$ , the following relation can be obtained in the overdamped regime:

$$\rho \ell_e^3 \epsilon = \frac{EI}{\ell_e \tau_b(\ell_e)} \Rightarrow \ell_e = \frac{B^{1/4}}{(\rho \mu \epsilon)^{1/8}}, \quad 11.$$

where  $\tau_b(\ell_e)$  is the bending relaxation time of a fiber with length  $\ell_e$  (see Equation 2). It is interesting to note that, even if  $\ell_e$  has a different physical interpretation for long and short fibers, it has the same expression (cf. Equation 9 for  $\mathcal{F} = 1$  and Equation 11). The power balance also allows prediction of the evolution of the mean curvature,  $\kappa$ , as function of the fiber length for intermediate flexibility (Brouzet et al. 2021):

$$\kappa \sim \frac{(\rho \mu \epsilon)^{1/2} l^3}{B} = \frac{l^3}{\ell_e^4}. \quad 12.$$

**4.2.2. Highly flexible fibers: 3D conformations.** The mean deformation of very flexible fibers, i.e., fibers with a length  $l \gg \ell_e$ , is tied to the turbulent fluctuations. Rosti et al. (2018) showed that tracking the fiber extremities in the underdamped regime allows measurement of the longitudinal structure function. This opens up new possibilities of using the fiber as a proxy for turbulence. It is also a natural extension of the work by Brizzolara et al. (2021), who proposed using the tumbling of rigid fibers to measure the transverse structure function. The possibility of measuring the structure function in the overdamped regime has not been considered yet. However, it has been shown that in such a regime the dependence of deformation to the turbulent fluctuations leads to a straightening of the fiber. Indeed, the mean curvature along the fiber length,  $\kappa(s)$ , increases from the extremities toward the center, where a maximum is reached, for flexible fibers ( $l \sim \ell_e$ ), as shown in **Figure 4a**. For very flexible fibers ( $l \gg \ell_e$ ), the curvature increases from the extremities, reaches a maximum at approximately one linear elastic length ( $s \simeq \ell_e$  and  $s \simeq l - \ell_e$ ), and decreases to a minimum at the center (Gay et al. 2018). Once again, a power balance can be used to understand this apparent stiffening. Due to fiber inextensibility, a local deformation caused by a small eddy will be accompanied by a global rearrangement of the fiber conformation. This rearrangement is at the origin of an additional viscous dissipation that scales as  $\mu \epsilon^{1/3} s^{4/3} B \kappa^3(s)$ , increasing with the fiber length  $l$ . For long fibers, the viscous dissipation can therefore be larger than bending and will then determine the amplitude of the mean curvature according to the following scaling relation:

$$\kappa(s) \sim \left(\frac{\rho}{B}\right)^{1/6} \epsilon^{1/9} s^{-2/9}. \quad 13.$$

In the Euler–Bernoulli equation, this nonlocal contribution appears in the tension term  $T$ . As detailed in Section 2, this term has two contributions: the tangential force,  $\int f_{\parallel}(s)ds$ , responsible for the stiffening, and a resistive term to bending,  $B\kappa^2$ , which acts as a nonlinear spring (Marheineke & Wegener 2007). In the overdamped regime, the transition from moderately flexible to highly

flexible fibers occurs when both the linear and nonlinear terms have the same amplitude:  $\kappa \sim L_v^{-1}$ , where  $L_v$  is a characteristic length scale referred to as nonlinear viscous elastic length, defined as

$$L_v = \frac{B^{3/10}}{\mu^{3/10} \epsilon^{1/10}}. \quad 14.$$

This definition has been validated by numerical simulations (Gay et al. 2018). In summary, for  $l \sim \ell_e$  the mean curvature increases when the length is increased as  $\kappa \sim l^3/\ell_e^4$ , while for  $l \gg L_v$  the mean curvature decreases when the fiber length is increased as  $\kappa \sim l^{-2/9}/\eta_K^{2/9} L_v^{5/9}$ . It might seem counterintuitive that in the nonlinear regime the mean curvature is smaller than in the linear regime. However, Olivieri et al. (2022a) studied the evolution of the mean of the maximum curvature  $\kappa_{\max}$  experienced by a fiber and found that the maximum curvature scales as  $\kappa_{\max}^l \sim (\mu \epsilon^{1/3} l^{10/3}/B)^\alpha$  with  $\alpha = 1$  in the linear regime and  $\alpha = 1/3$  in the nonlinear regime. Then, even if the exponent for a very flexible fiber is lower than the one for the linear regime, it is still positive and therefore the mean maximum curvature continuously increases, as shown in **Figure 4b**. The different values of the exponent can be found by balancing the viscous forcing and the linear or nonlinear elastic term in Equation 1. A similar evolution for the mean of the maximum curvature has been observed in the underdamped regime (Olivieri et al. 2022b). However, inertia and the presence of bending waves make the problem more complex to analyze (Audoly & Neukirch 2005). Moreover, in the underdamped regime, the transition length scale between the two regimes of deformations has been shown to be equal to (Rosti et al. 2018)

$$L_i = \frac{B^{3/8}}{\epsilon^{1/4} (\rho_f d^2)^{3/8}}. \quad 15.$$

This nonlinear inertial length has been interpreted as the one for which the forcing timescale and the period of oscillation are equal. Note that this temporal argument in the overdamped regime can also be used to define the transition length scale and leads to the same nonlinear viscous length  $L_v$  defined previously. Finally, it is important to remark that fiber deformation, as well as its overall dynamics, is also modulated by the density difference between the fiber and fluid, which has a twofold effect. First, the density mismatch affects the dynamical regime that characterizes the fiber (overdamped or underdamped) (see Section 2). Second, it controls the period of oscillation  $T_o$  (see Equation 5), which determines the two subregimes present in the underdamped regime (see **Figure 4**).

## 5. FIBER MOTION

Fiber dispersion in a turbulent flow has been investigated mostly for the case of rigid fibers modeled as rods or ellipsoids, focusing on phenomena such as preferential alignment and preferential concentration (Marchioli et al. 2016, Voth & Soldati 2017). The understanding of these phenomena is rather complete for sub-Kolmogorov fibers. However, much less is known for long fibers, especially for lengths comparable to the flow scales within the inertial range, a limit that is relevant for the case of flexible fibers and has been addressed only recently (Chiarini et al. 2024). In this section, we survey the phenomenology of the motion of flexible fibers in turbulence, specifically addressing the features that characterize their collective dispersion behavior. In fact, the settling of flexible heavy fibers in turbulence has received little attention (Banaei et al. 2020a): This is clearly an area ripe for future development.

### 5.1. Fiber Spatial Distribution

The spatial distribution attained by fibers in a turbulent flow is generally nonuniform and modulated by several concurrent factors, particularly fiber inertia. Inertial fibers tend to concentrate

## CLUSTERING AND CAUSTICS

In particle-laden flows, one of the cluster formation mechanisms is clustering by caustics. Caustics are phase-space singularities that, akin to caustics in geometrical optics, result in anomalous particle number density fields and large relative velocities at small separations, causing the spatial continuum descriptions of the inertial particle velocity field to fail (Falkovich et al. 2002, Wilkinson & Mehlig 2005).

preferentially and form clusters within the flow. In confined flows, their distribution is also nonuniform along the wall-normal direction, possibly leading to segregation in the wall region. These mechanisms, which have been widely investigated for spherical particles (Soldati & Marchioli 2009), are examined next to highlight the distinctiveness of flexible fibers.

**5.1.1. Preferential concentration and clustering.** Up to now, the analysis of preferential concentration and clustering has been carried out in the limit of dilute suspensions, in which fiber–fiber interactions due to collisions are negligible. In the case of homogeneous isotropic turbulence (HIT), the spatial distribution of long fibers is associated with the preferential sampling of vortical flow structures, provided the fibers are longer than the dissipation scale but not much longer than the vortex tubes (Picardo et al. 2018, 2020). Bending stiffness has no effect because the fibers do not need to coil in order to thread a vortex tube and align with its axis. This is not true in 2D turbulence, where bending stiffness is found to prevent coiling and reduce preferential sampling (Picardo et al. 2018). Note that clustering in 2D flows is dependent on both the Stokes number and the fiber aspect ratio, and it is strongly correlated with the formation of velocity caustics, namely, singularities in which fibers are focused in thin filaments that resemble the optical caustics formed by deflection of sunlight by water waves (Martínez et al. 2017) (see the sidebar titled Clustering and Caustics). In the case of extensible fibers that can be stretched out by the flow, these also preferentially sample the intense, tubular, vortex filaments of 3D turbulence, particularly for lengths up to inertial-range scales. Such fibers extend in vortical regions and follow axially stretched tubular vortices by aligning with their axes (Picardo et al. 2020, Singh et al. 2020).

Olivieri et al. (2022b) observed a systematic increase of clustering at increasing fiber flexibility (i.e., decreasing the bending stiffness) and, as expected, for inertial fibers. This clustering is always associated with a preferential alignment between the local orientation of the fibers and the strain rate principal directions: Both the alignment with the first or second principal direction (namely, the direction of maximum extension or intermediate extension/compression, respectively) and the antialignment with the third principal direction (maximum compression direction) typically increase when the fibers become more rigid; this increase is also observed when moving from heavy to neutrally buoyant fibers. Similar conclusions were obtained for the case of a wall-bounded flow by Dotto & Marchioli (2019) and Dotto et al. (2020), who observed that flexible fibers exhibit a stronger tendency than rigid fibers to accumulate in the very-near-wall region, where they appear to be trapped by the same inertia-driven mechanisms that govern the preferential concentration of spherical particles and rigid fibers in bounded flows. In such regions, the bending of flexible fibers increases as inertia decreases, and fiber deformation appears to be controlled by mean shear and turbulent Reynolds stresses. Preferential segregation into low-speed streaks and preferential orientation in the mean flow direction are also observed, as discussed in Section 5.1.2.

**5.1.2. Wall accumulation and segregation.** In wall-bounded turbulence, fibers tumble and collide with solid boundaries, bouncing off with an impulse that propels them toward the center of the flow, similar to pole vaulting. For short fibers, the resulting spatial distribution is determined

by a balance between this bounce-off drift and the turbophoretic drift (Marchioli & Soldati 2002, Bec et al. 2024) that controls wall accumulation for inertial particles, especially those with sub-Kolmogorov size. As shown by Dotto & Marchioli (2019) and Dotto et al. (2020), flexible fibers with a length significantly smaller than the inertial subrange of turbulence still undergo a net wallward drift, but the peak of near-wall concentration is much weaker compared to spherical particles (Marchioli & Soldati 2002, Bec et al. 2024) and rigid fibers (Marchioli et al. 2010, Dhas & Marchioli 2025). Sub-Kolmogorov spherical particles can penetrate much deeper inside the viscous sublayer, and this facilitates their long-term trapping into low-speed fluid streaks (Dotto & Marchioli 2019, Di Giusto & Marchioli 2022). Super-Kolmogorov spherical particles cannot do that, and their wall accumulation is limited by an excluded-volume geometric effect, which prevents the formation of strong accumulation regions due to the misalignment between fiber orientation and the straining regions of the flow. In principle, rigid fibers could execute efficient pole vaulting, but their capability to escape is limited by the tendency to enter the near-wall layer with a shallow angle and to align parallel to the wall. Remarkably, wall accumulation is not observed for long fibers, which are more efficient than short fibers in exploiting the bounce-off drift allowed by pole vaulting and thus exhibit a stronger tendency to migrate away from the walls. This dynamics produces depleted regions near the boundaries and more concentrated regions in the bulk. As shown by Bec et al. (2024), these higher concentrations in the channel center result in a greater net flux of fibers than what was initially imposed by the fluid, with the effect being more pronounced as the fiber length increases. It should be noted that long fibers can sample different regions of the flow simultaneously; namely, portions of the fiber located at different wall distances experience different average fluid velocities. For inextensible fibers, this implies that portions located closer to the channel center, where the mean velocity is higher, tend to pull the whole fiber. On the other hand, portions closer to the walls, where the mean velocity is lower, tend to slow it down. This results in a higher fiber streamwise velocity than the fluid near the walls and lower in the center, as observed in **Figure 5**.

## 5.2. Fiber Preferential Alignment

Preferential alignment has been investigated in terms of alignment with the stretching and compressing directions within the flow (mostly in HIT) but also in terms of alignment with the flow directions (in wall-bounded turbulence). Results obtained in HIT by Olivieri et al. (2022b) indicate that the vorticity is mostly aligned with the intermediate eigenvector and orthogonal to the direction of maximum compression, i.e., the third eigenvector, while only a minimal departure is observed for the alignment with the first eigenvector, corresponding to the direction of maximum extension. The main difference that can be observed between neutrally buoyant fibers and heavier-than-fluid fibers is the mild attenuation of the alignment of vorticity with the intermediate eigenvector in the latter case, as well as a weakening of the preferential alignment of fibers with the strain rate. Similar behavior is observed in viscoelastic turbulence, in which flexible fibers interact with stretching polymers (Aswathy & Rosti 2024): The neutrally buoyant fibers show a higher alignment with the polymer stretching directions compared to the denser ones. In wall-bounded turbulence, fibers tend to preferentially align with the streamwise flow direction and perpendicular to the mean shear, this trend being more evident for longer fibers. Away from the walls, a weaker preferential alignment is observed because the flow becomes more homogeneous and isotropic (Dotto & Marchioli 2019, Dotto et al. 2020).

## 5.3. Fiber Rotation

Similarly to rigid fibers (Shin & Koch 2005, Oehmke et al. 2021), the rotation of a flexible fiber is related closely to its orientational dynamics and tendency to align preferentially with the flow. Up

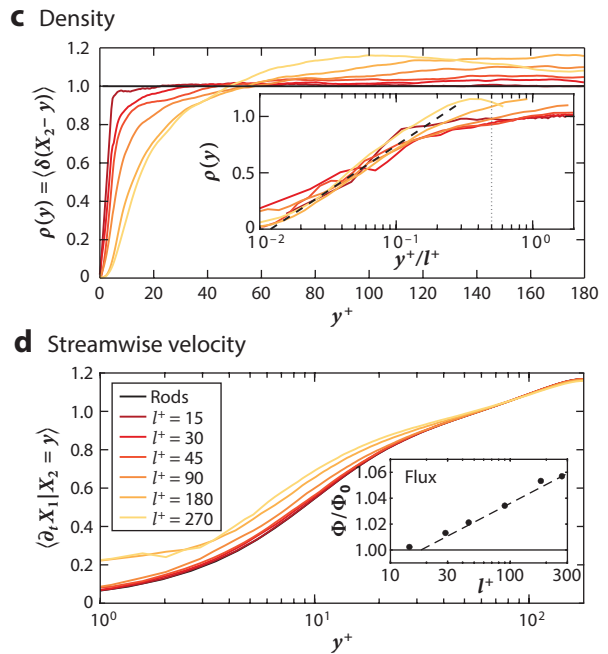
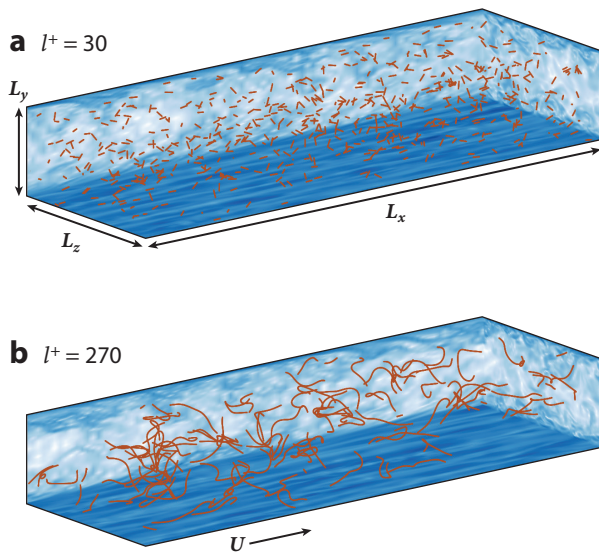


**Figure 5**

(a,b) Instantaneous distribution of flexible fibers with lengths  $l^+ = 30$  and  $l^+ = 270$  in wall units. The color map shows the modulus of fluid vorticity in the bounding planes. (c) Average fiber number density as a function of the distance to the wall,  $y^+$ , at varying fiber lengths, also shown as a function of  $y^+/l^+$  in the inset, where the dashed line shows the  $\log l^+$  scaling. (d) Average fiber velocity in the streamwise direction as a function of  $y^+$ . The inset shows the normalized fiber fluxes, obtained by combining the concentration and velocity profiles: The logarithmic scaling (dashed line) shows a slight increase of the flux for fibers whose lengths are within the log-layer of the wall. Figure adapted from Bec et al. (2024).

to now, the rotation of flexible fibers has been investigated for wall-bounded turbulence, where the flow anisotropy plays a major role in determining fiber tumbling and spinning. Dhas & Marchioli (2025) recently showed that fibers with negligible inertia tend to experience higher tumbling and spinning rates close to the wall than near the channel center. Further, longer fibers exhibit higher rotation rates, whereas the introduction of rigidity tends to have the opposite effect. This is associated with slower changes in orientation experienced by the flexible fibers, in view of their tendency to migrate away from the wall, compared to their rigid counterparts, which tend to stay closer to the wall and are thus subject to a stronger mean shear. However, the rotation of the longer fibers is found to be less sensitive to their flexibility/rigidity as they move and orient themselves similarly, irrespective of their bending stiffness. The rotation rates of the fibers exhibit a clear dependence on flexibility and length in the bulk of the flow. The effect of length vanishes in the case of rigid fibers. Owing to the strong turbulence fluctuations that occur close to the wall and to fiber-wall collisions, fibers in that region tend to tumble and spin at rates significantly higher than those closer to the channel center.

## 6. THE ROLE OF FLEXIBILITY ON FIBER-TURBULENCE INTERACTIONS

The collective dynamics of flexible fibers in fluid flows can lead to macroscopic effects that are of relevance in a number of situations of practical interest. Notable examples are fractionation

### Tumbling and spinning:

the rotation modes of an axisymmetric particle are naturally decomposed into two components perpendicular to the symmetry axis, called tumbling, and one component along the symmetry axis, called spinning or drilling

(Lundell et al. 2011) and entanglement/flocculation (Switzer & Klingenberg 2004, Cui & Grace 2007). Of the many macroscopic phenomena that could be addressed, here we focus on two problems that have attracted the attention of researchers and for which progress has been made in connecting microscopic fiber dynamics to the macroscopic phenomena of interest: fragmentation and turbulence modulation.

## 6.1. Fragmentation

The discussion so far has focused on fibers that exhibit a Hookean behavior and undergo linear elastic deformations that satisfy the condition  $\kappa d \ll 1$ . In this section, we address the fragmentation of brittle fibers that break when undergoing large deformations. For a brittle fiber, breakup occurs as soon as the applied stress causing deformation reaches a threshold, called the yield stress  $\sigma_b$ . This kind of particle is a good model to investigate the fragmentation of microplastics in the sea, which have been weathered by UV, salt, ozone, and microorganisms. In numerical simulations, this parameter can be adjusted to explore a range of regimes from tough to very fragile materials. In experiments, the yield stress is a distributed value, and its mean can be varied by changing the material of the fiber and/or the density of defects (Brouzet et al. 2021). So far, only the fragmentation of fibers in the overdamped regime has been investigated. As discussed in Section 2, the modes of deformation and the statistics differ for short and long fibers, leading to distinct breakup scenarios.

As short fibers preferentially align with the elongational component of the rate-of-strain tensor, they are mainly stretched by the flow. In this case, the stress is equal to zero at the fiber extremities and increases quadratically to reach a maximum value at the fiber center. When the stress exceeds the yield stress, the fiber breaks into two fragments of equal length (Allende et al. 2020). Another breaking mode is observed when short fibers align with the compressive direction of the rate-of-strain tensor triggered by the buckling instability. For this type of deformation, the stress  $\sigma$  is proportional to the local curvature  $\kappa$ , i.e.,  $\sigma \sim \kappa d$ . In this configuration, the fiber can break into several fragments, with the number of fragments depending on the excited buckling mode, the local intensity of the velocity gradient, and the stiffness of the fiber (Allende et al. 2020).

For long fibers, three scenarios have been identified, based on the fiber brittleness. The first one corresponds to fibers with a high yield strain, which requires curvatures higher than the maximum curvature a flexible fiber can sustain before being broken. The second scenario involves very fragile fibers that can break at curvatures much smaller than  $1/\ell_e$ , thus forming fragments much smaller than the elastic length. In this case, the typical fragment size is expected to be given by the mean curvature of the fiber, which scales as  $\kappa_{\max} \sim l^3/\ell_e^4$ . The third scenario corresponds to an intermediate regime in which the maximum curvature before breaking is  $\kappa_{\max} \sim 1/\ell_e$ . In this context, Brouzet et al. (2021) modeled the evolution of the fragment size distribution over time using a Smoluchowski equation:

$$\partial_t n_\ell = -p(\ell)n_\ell + \int 2p(\ell_>)\gamma(\ell, \ell_>) d\ell_>, \quad 16.$$

where  $n_\ell$  is the number of fragments of size  $\ell$ ,  $p(\ell)$  is the probability that a fiber of length  $\ell$  breaks, and  $\gamma(\ell, \ell_>)$  is the probability that a fiber of length  $\ell_>$  breaks into two parts, one of length  $\ell$  and one of length  $\ell_> - \ell$ . The probability  $p(\ell)$  can be estimated using the curvature distribution, while  $\gamma(\ell, \ell_>)$  can be derived from the evolution of the mean curvature along the fiber length (Brouzet et al. 2021). Ultimately, the final distribution corresponds to a relatively peaked distribution with a maximum length of the order of  $\ell_e$ . The research on the fragmentation of long fibers has, so far, been focused on the fragment size distribution, and the evaluation of the fragmentation rate is still an open question.

## 6.2. Turbulence Modulation

Most research on the dynamics of particles dispersed in turbulence has focused on dilute suspensions, in which the flow is unaffected by the presence of the dispersed phase. In this situation, a one-way coupling approach can be adopted, which greatly simplifies the modeling of the problem. However, for relatively high concentrations, one must take into account the two-way coupled problem: In addition to the particles being transported and distorted by the flow, the flow is also changed by their backreaction, because of the no-slip condition at the particle surface (Balachandar & Eaton 2010, Maxey 2017, Brandt & Coletti 2022). Focusing on the specific case of anisotropic particles and fibers, relatively few studies have examined the modulation of turbulence under nondilute conditions (Andersson et al. 2012; Ardekani et al. 2017; Olivieri et al. 2020, 2021, 2022b), showing a significant deviation from the conventional phenomenology seen for a strictly Newtonian fluid. More specifically, Olivieri et al. (2021, 2022b) methodically explained how the backreaction of the dispersed phase impacts the macroscopic behavior of the carrier flow, demonstrating a general depletion of turbulent kinetic energy that is mirrored by the (decreasing) microscale Reynolds number of the flow. The mass fraction of the suspension, given by the ratio of the mass of the suspended fibers to the total mass of the suspension (which is thus a combination of the density ratio and volume fraction), rather than other factors like the number density, controls the backreaction, noting that at number densities corresponding to the so-called dilute regime (Butler & Snook 2018), the backreaction effect can already be nonnegligible. The energy spectra, reported in **Figure 6**, show two robust features when the mass fraction increases: a relative increase in the small-scale energy content and an overall large-scale energy depletion. The energy fluxes in Fourier space (see the sidebar titled Multiscale Energy Balance) provide a good explanation for this evidence: As the mass fraction increases, the nonlinear term is suppressed and the energy transfer directly related to the fluid–solid coupling becomes more significant. Surprisingly, the flexibility of the fibers seems to have a rather small, but consistent, impact, with a weaker backreaction for more flexible fibers. From the physical viewpoint, a more relaxed flow–structure coupling (i.e., fibers are more responsive to the action of the flow) results from greater flexibility (i.e., reducing  $B$ ), which is reflected in a less noticeable backreaction when compared to the rigid case. In general, flexibility may be claimed to be of secondary importance in the modulation of the carrier flow because the variation with  $\gamma$  seems to be quite modest.

Olivieri et al. (2022a) and Cannon et al. (2024) discovered that the drop in the turbulent kinetic energy and microscale Reynolds number with an increasing mass fraction is comparable to that produced by spherical particles of the same length. The authors demonstrated that the sphere diameter or fiber length is the representative length scale at which the fluid–solid coupling is prominent for both types of dispersed objects. However, while the backreaction for finite-size spherical objects is usually limited to relatively large scales, with a small change of the higher-wavenumber inertial and viscous subrange, the complete energy spectrum is altered with finite-size fibers, as a result of their ability to transport energy down to the lowest scales of the flow. This difference can be simply understood by considering that immersed objects subtract energy from the flow by means of hydrodynamic drag and then reinject it through their wakes. Spheres produce a turbulent wake that contributes to the classical energy cascade, since this occurs entirely within the inertial subrange. The transfer for fibers occurs instead at much smaller scales, where viscosity takes over, thus inhibiting the contribution of the nonlinear term. Cannon et al. (2024) examined the vorticity and shear of local flow structures to determine their shape. In addition to producing strong vortical and shearing structures that counteract the typical vortex stretching behavior, the authors discovered that the fibers increase local shear and dissipation in structures that have dimensions larger than one but less than two, a possible source of the increased flow

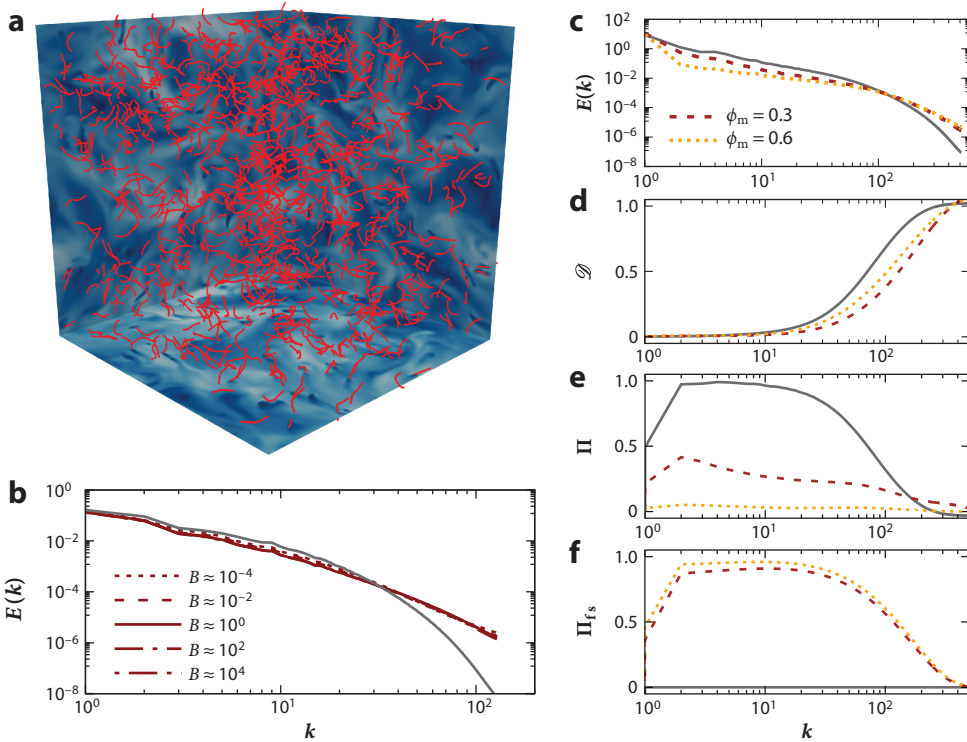


**Figure 6**

(a) Snapshot from direct numerical simulation of finite-size flexible fibers (*in red*) dispersed in homogeneous isotropic turbulence. The length of the fiber is within the inertial range of scales. (b) The energy spectra for a suspension of fibers with different bending modulus,  $B$ . (c) Energy spectra, (d) fluid dissipation, (e) nonlinear energy flux, and (f) fluid–solid interaction contribution for different values of the mass fraction,  $\phi_m$ . In panels b–f, the gray curves correspond to the unladen case. Figure adapted from Olivieri et al. (2022b) (CC BY 4.0).

intermittency. Cannon et al. (2024) also examined how the Reynolds number affected the modulation of turbulence: Fibers modulate turbulence even in the weakest turbulent flows ( $Re \rightarrow 0$ ), with the majority of observables converging to the single-phase result as  $Re \rightarrow \infty$ , except for the modulation of turbulent kinetic energy, in which the Reynolds number has little to no effect. Note

## MULTISCALE ENERGY BALANCE

The scale-by-scale energy transfer for a two-phase flow can be written as

$$\mathcal{P}(k) + \Pi(k) + \Pi_{fs}(k) + \mathcal{D}(k) = \epsilon, \quad \text{SB4.}$$

where the various terms appearing on the left-hand side are the production rate  $\mathcal{P}$  (here associated with the external forcing used to sustain the flow and typically acting only at the largest scales, i.e., low wavenumbers), the energy flux  $\Pi$  associated with the nonlinear term, the energy flux  $\Pi_{fs}$  associated with the fluid–solid coupling, and the viscous dissipation  $\mathcal{D}$ . In the single-phase case, when  $\Pi_{fs} \equiv 0$ , the dominant terms in the balance are the nonlinear term  $\Pi$  and the viscous dissipation  $\mathcal{D}$  when approaching the lowest and highest wavenumbers, respectively. See Pope (2001) for a full derivation of the single-phase equation and Olivieri et al. (2020) for the extension to the case with fibers.

that the multiscale effect carried by the fibers in a turbulent flow has also been found in the case of canopy flows, when the fibers are clamped to the wall (Monti et al. 2023; Foggi Rota et al. 2024a,b, 2025).

When considering channel flows, only a few studies have examined the potential reduction of turbulent friction losses by the addition of fibers (Paschkewitz et al. 2004, 2005; Gillissen et al. 2008; Moosaie & Manhart 2013; Di Giusto & Marchioli 2022), inspired by the vast amount of work done with polymers (see, e.g., White & Mungal 2008, Benzi & Ching 2018), with fibers providing little drag reduction or requiring significantly higher concentrations to achieve the same drag reduction. Paschkewitz et al. (2004) were among the first to investigate the drag reduction caused by rigid neutrally buoyant fibers, modeling their influence with lengths significantly shorter than all scales of turbulent flow. They found that the fibers weaken and enlarge the near-wall vortex structures and reduce drag by producing a force contrary to the Newtonian acceleration. The effectiveness of short stiff rods in reducing drag was experimentally proven by Paschkewitz et al. (2005), who reported a 10% reduction in drag. In light of these encouraging findings, Moosaie & Manhart (2013) created a two-way coupling modeling method for a diluted suspension of rigid fibers and further validated the previous findings. In a more recent study, Di Giusto & Marchioli (2022) discovered that employing substantially longer fibers can similarly reduce drag in a turbulent channel flow, with smaller volume fractions.

## 7. CONCLUSIONS AND PERSPECTIVES

Flexible fibers in turbulence present a rich source of problems in terms of local and nonlocal interactions with the fluid. These interactions result in a number of complex phenomena that can only be investigated using sophisticated experimental and numerical techniques. Also complicated are the theories through which fiber dynamics can be understood and modeled. To close our review, we summarize the main takeaways and future issues.

### SUMMARY POINTS

1. Flexible fibers in high-Reynolds-number flows are found in many environmental and industrial problems of practical interest and are receiving growing attention from the multiphase flow community. To study these problems, it is possible to leverage the experimental and numerical tools that have been developed for the investigation of elongated nonspherical particles (rigid fibers, in particular), extending their applicability to include flexibility effects.
2. Flexibility can be characterized by two main length scales: the linear elastic length,  $\ell_e$ , and the nonlinear viscous elastic length,  $L_v$ . These scales can be used to discriminate between the different fiber deformation regimes that characterize fiber motion. In particular,  $L_v$  represents a threshold between smooth (C-shaped or U-shaped) deformations and more complex deformations.
3. Flexibility has an effect on macroscopic phenomena such as wall accumulation and preferential concentration, which exhibit both qualitative and quantitative differences with respect to the case of spherical particles and rigid fibers. This happens because the sampling of the turbulent flow by the fibers is governed by nonlocal dynamics associated with their length and stiffness, differently from rigid fibers that are governed by local dissipative dynamics.

4. Long fibers experience a varying flow field along their length. When fibers are rigid, their inability to deform acts like a coarse-graining high-pass filter that makes fibers insensitive to the small scales of the flow. Flexibility removes this filter and allows fibers to respond to the small scales. This implies that the local features of the flow play a role in determining the dynamics of individual fibers.
5. While flexibility is a key feature to understand the fiber dynamics, the effect of the fibers on the turbulent flow seems to be less affected by the fiber deformation, where the mass and volume fraction are the most determinant factors.

## FUTURE ISSUES

1. An important aspect that requires attention has to do with the lack of uniformity of the averaging procedures adopted to compute the statistics and even the definition of important quantities such as the fiber response time and Reynolds number. Different averaging procedures and definitions are found in the literature, making comparison of results difficult or even misleading. This review offers a first step toward a unifying framework, but additional efforts are certainly needed.
2. Generally speaking, the macroscopic consequences of fiber dynamics in turbulence are still poorly understood. This is especially true for flexible fibers, for which only a minor proportion of the parameter space has been explored so far. As a consequence, there is a knowledge gap that prevents connecting applications to the fundamental governing mechanisms.
3. Models capable of handling realistic calculations of the full shape of the fiber and its aerodynamic coefficients are required to boost the reliability of numerical simulations. Also needed are models that can deal with shape asymmetries (e.g., curved fibers with fore–aft asymmetry) and account for their effect on the inertial torques and angular dynamics of the fibers.
4. A particular need in experiments is the ability to relate the dynamics of individual particles to macroscopic effects such as turbulence modulation (possibly including the effect of fiber extensibility) or rheological effects in dense suspensions.
5. For problems involving inertial flexible fibers in turbulence, little is known about how their dynamics are altered in finite Froude number conditions (i.e., when the gravitational forces are not negligible).
6. Future effort should also be devoted to the analysis of deformable objects with shapes different from the elongated cylindrical fibers addressed in this review, for which stretching and twisting can play an important role (e.g., flexible disks in turbulence). To tackle this problem, experimental techniques are already being developed but no suitable generalization of the discrete or continuous approaches discussed in this review has been developed yet.

## DISCLOSURE STATEMENT

The authors are not aware of any affiliations, memberships, funding, or financial holdings that might be perceived as affecting the objectivity of this review.

## ACKNOWLEDGMENTS

C.M. gratefully acknowledges financial support from the European Union's NextGenerationEU PRIN 2022 ("Next-generation multiscale modelling of dense emulsions for enhanced multiphase flow processes," 20229WJBPS - E53D23002940006). M.E.R. is supported by the Okinawa Institute of Science and Technology Graduate University, with subsidy funding from the Cabinet Office, Government of Japan. G.V. acknowledges financial support from the French National Research Agency (ANR) within the framework of the NetFlex project (ANR-21-486 CE30-0040).

## LITERATURE CITED

- Agrawal A, Ramalingam S, Taguchi Y, Chari V. 2012. A theory of multi-layer flat refractive geometry. In *2012 IEEE Conference on Computer Vision and Pattern Recognition*. IEEE
- Agrawal V, Kulachenko A, Scapin N, Tammisola O, Brandt L. 2024. An efficient isogeometric/finite-difference immersed boundary method for the fluid–structure interactions of slender flexible structures. *Comput. Methods Appl. Mech. Eng.* 418:116495
- Allende S, Henry C, Bec J. 2018. Stretching and buckling of small elastic fibers in turbulence. *Phys. Rev. Lett.* 121:154501
- Allende S, Henry C, Bec J. 2020. Dynamics and fragmentation of small inextensible fibres in turbulence. *Philos. Trans. R. Soc. A* 378(2175):20190398
- Andersson H, Celledoni E, Ohm L, Owren B, Tapley B. 2021. An integral model based on slender body theory, with applications to curved rigid fibers. *Phys. Fluids* 33:041904
- Andersson H, Zhao L, Barri M. 2012. Torque-coupling and particle–turbulence interactions. *J. Fluid Mech.* 696:319–29
- Andrić J, Fredriksson S, Lindström S, Sasic S, Nilsson H. 2013. A study of a flexible fiber model and its behavior in DNS of turbulent channel flow. *Acta Mech.* 224:2359
- Andrić J, Lindström S, Sasic S, Nilsson H. 2014. Rheological properties of dilute suspensions of rigid and flexible fibers. *J. Non-Newton. Fluid Mech.* 212:36–46
- Ardekani M, Costa P, Breugem W, Picano F, Brandt L. 2017. Drag reduction in turbulent channel flow laden with finite-size oblate spheroids. *J. Fluid Mech.* 816:43–70
- Aswathy M, Rosti ME. 2024. The dynamics of fibres dispersed in viscoelastic turbulent flows. *J. Fluid Mech.* 984:A72
- Audoly B, Neukirch S. 2005. Fragmentation of rods by cascading cracks: why spaghetti does not break in half. *Phys. Rev. Lett.* 959:095505
- Audoly B, Pomeau Y. 2010. *Elasticity and Geometry*. Oxford University Press
- Balachandar S, Eaton J. 2010. Turbulent dispersed multiphase flow. *Annu. Rev. Fluid Mech.* 42:111–33
- Banaei A, Rahmani M, Martínez D, Brandt L. 2020a. Inertial settling of flexible fiber suspensions. *Phys. Rev. Fluids* 5(2):024301
- Banaei A, Rosti ME, Brandt L. 2020b. Numerical study of filament suspensions at finite inertia. *J. Fluid Mech.* 882:A5
- Batchelor G. 1970. Slender-body theory for particles of arbitrary cross-section in Stokes flow. *J. Fluid Mech.* 44(3):419–40
- Bec J, Brouzet C, Henry C. 2024. Enhanced transport of flexible fibers by pole vaulting in turbulent wall-bounded flow. *Phys. Rev. Fluids* 9:L062501
- Belden J. 2013. Calibration of multi-camera systems with refractive interfaces. *Exp. Fluids* 54:1463
- Benzi R, Ching E. 2018. Polymers in fluid flows. *Annu. Rev. Condens. Matter Phys.* 9:163–81
- Bergfreund J, Wobill C, Lebreton L, Windhab E, Evers F, et al. 2024. Impact of microplastic pollution on breaking waves. *Phys. Fluids* 36:072108
- Bhowmick T, Seesing J, Gustavsson K, Guettler J, Wang Y, et al. 2024. Inertia induces strong orientation fluctuations of non-spherical atmospheric particles. *Phys. Rev. Lett.* 132:034101
- Brandt L, Coletti F. 2022. Particle-laden turbulence: progress and perspectives. *Annu. Rev. Fluid Mech.* 54:159–89

- Brizzolara S, Rosti ME, Olivieri S, Brandt L, Holzner M, Mazzino A. 2021. Fiber tracking velocimetry for two-point statistics of turbulence. *Phys. Rev. X* 11(3):031060
- Brouzet C, Guiné R, Dalbe MJ, Favier B, Vandenberghe N, et al. 2021. A laboratory model for plastic fragmentation in the turbulent ocean. *Phys. Rev. Fluids* 6:024601
- Brouzet C, Verhille G, Le Gal P. 2014. Flexible fiber in a turbulent flow: a macroscopic polymer. *Phys. Rev. Lett.* 112:074501
- Butler J, Snook B. 2018. Microstructural dynamics and rheology of suspensions of rigid fibers. *Annu. Rev. Fluid Mech.* 50:299–318
- Candelier F, Gustavsson K, Sharma P, Sundberg L, Pumis A, et al. 2024. Torques on curved atmospheric fibres. *Phys. Rev. Res.* 7:013179
- Cannon I, Olivieri S, Rosti ME. 2024. Spheres and fibers in turbulent flows at various Reynolds numbers. *Phys. Rev. Fluids* 9(6):064301
- Chen Z, Liu Y, Sung H. 2024. Enhancement of heat transfer by a buckled flexible filament in a channel flow. *Int. J. Heat Mass Transf.* 224:125364
- Chiarini A, Rosti ME, Mazzino A. 2024. Dynamics and applications of finite-size fibre-like objects in turbulent flows. *Eur. J. Mech. B Fluids* 108:104–18
- Cox RG. 1970. The motion of long slender bodies in a viscous fluid. Part 1. General theory. *J. Fluid Mech.* 44:791–810
- Cox RG. 1971. The motion of long slender bodies in a viscous fluid. Part 2. Shear flow. *J. Fluid Mech.* 45:625–57
- Cui H, Grace J. 2007. Flow of pulp fibre suspension and slurries: a review. *Int. J. Multiphase Flow* 33:921–34
- Delmotte B, Climent E, Plouraboué F. 2015. A general formulation of bead models applied to flexible fibers and active filaments at low Reynolds number. *J. Comput. Phys.* 286:14–37
- Dhas D, Marchioli C. 2025. Orientational dynamics of long flexible fibers in wall-bounded turbulence. *J. Fluids Eng.* 147(7):071102
- Di Giusto D, Bergougnoux L, Marchioli C, Guazzelli E. 2024. Influence of small inertia on Jeffery orbits. *J. Fluid Mech.* 979:A42
- Di Giusto D, Marchioli C. 2022. Turbulence modulation by slender fibers. *Fluids* 7(8):255
- Doi M, Edwards S. 1986. *The Theory of Polymer Dynamics*. Oxford University Press
- Dotto D, Marchioli C. 2019. Orientation, distribution, and deformation of inertial flexible fibers in turbulent channel flow. *Acta Mech.* 230:597–621
- Dotto D, Soldati A, Marchioli C. 2020. Deformation of flexible fibers in turbulent channel flow. *Meccanica* 55:343–56
- du Roure O, Lindner A, Nazockdast E, Shelley M. 2019. Dynamics of flexible fibers in viscous flows and fluids. *Annu. Rev. Fluid Mech.* 51:539–72
- Falkovich G, Fouxon A, Stepanov MG. 2002. Acceleration of rain initiation by cloud turbulence. *Nature* 419:151–54
- Faugeras O, Luong QT. 2001. *The Geometry of Multiple Images*. MIT Press
- Favier J, Revell A, Pinelli A. 2014. A Lattice Boltzmann-immersed boundary method to simulate the fluid interaction with moving and slender flexible objects. *J. Comput. Phys.* 261:145–61
- Foggi Rota G, Chiarini A, Rosti ME. 2025. Reconfiguration and dynamics of clamped fibers under finite-amplitude surface gravity waves. *Phys. Rev. Fluids* 10(1):014301
- Foggi Rota G, Koseki M, Agrawal R, Rosti ME. 2024a. Forced and natural dynamics of a clamped flexible fiber in wall turbulence. *Phys. Rev. Fluids* 9:L012601
- Foggi Rota G, Monti A, Olivieri S, Rosti ME. 2024b. Dynamics and fluid–structure interaction in turbulent flows within and above flexible canopies. *J. Fluid Mech.* 989:A11
- Gay A, Favier B, Verhille G. 2018. Characterisation of flexible fibre deformations in turbulence. *Europhys. Lett.* 123:24001
- Gillissen J, Boersma B, Mortensen P, Anderson H. 2008. Fibre-induced drag reduction. *J. Fluid Mech.* 602:209–18

- Giurgiu V, Caridi G, Alipour M, De Paoli M, Soldati A. 2023. The TU Wien Turbulent Water Channel: flow control loop and three-dimensional reconstruction of anisotropic particle dynamics. *Rev. Sci. Instrum.* 94:095101
- Giurgiu V, Caridi G, De Paoli M, Soldati A. 2024. Full rotational dynamics of plastic microfibers in turbulence. *Phys. Rev. Lett.* 132:054101
- Goldstein D, Handler R, Sirovich L. 1993. Modeling a no-slip flow boundary with an external force field. *J. Comp. Phys.* 105(2):354–66
- Huang W, Shin S, Sung H. 2007. Simulation of flexible filaments in a uniform flow by the immersed boundary method. *J. Comp. Phys.* 226(2):2206–28
- Kamal C, Lauga E. 2023. Resistive-force theory of slender bodies in viscosity gradients turbulence. *J. Fluid Mech.* 963:A24
- Kim S, Karrila S. 1991. *Microhydrodynamics: Principles and Selected Applications*. Butterworth-Heinemann
- Kim T, Kim J, Jeong O. 2011. Measurement of nonlinear mechanical properties of PDMS elastomer. *Microelectron. Eng.* 88:1982–85
- Kunhappan D, Harthong B, Chareyre B, Balarac G, Dumont P. 2017. Numerical modelling of high aspect ratio flexible fibers in inertial flows. *Phys. Fluids* 29:093302
- Landau L, Lifshitz E. 1959. *Theory of Elasticity*. Pergamon Press
- Lindström S, Uesaka T. 2007. Simulation of the motion of flexible fibers in viscous fluid flow. *Phys. Fluids* 19:113307
- Lindström S, Uesaka T. 2009. A numerical investigation of the rheology of sheared fiber suspensions. *Phys. Fluids* 21:083301
- Lundell F, Söderberg L, Alfredsson P. 2011. Fluid mechanics of papermaking. *Annu. Rev. Fluid Mech.* 43:195–217
- Machicoane N, Aliseda A, Volk R, Bourgoin M. 2019. A simplified and versatile calibration method for multi-camera optical systems in 3D particle imaging. *Rev. Sci. Instrum.* 90(3):035112
- Marchetti B, Raspa V, Lindner A, du Roure O, Bergougoux L, et al. 2018. The deformation of a flexible fiber settling in a quiescent viscous fluid. *Phys. Rev. Fluids* 3:104102
- Marchioli C, Fantoni M, Soldati A. 2010. Orientation, distribution and deposition of elongated, inertial fibers in turbulent channel flow. *Phys. Fluids* 22(3):033301
- Marchioli C, Soldati A. 2002. Mechanisms for particle transfer and segregation in a turbulent boundary layer. *J. Fluid Mech.* 468:283–315
- Marchioli C, Zhao L, Andersson H. 2016. On the relative rotational motion between rigid fibers and fluid in turbulent channel flow. *Phys. Fluids* 28(1):013301
- Marheineke N, Wegener R. 2007. Modeling and application of a stochastic drag for fibers in turbulent flows. *Int. J. Multiphase Flow* 37(2):136–48
- Martínez M, Vernet A, Pallares J. 2017. Clustering of long flexible fibers in two-dimensional flow fields for different Stokes numbers. *Int. J. Heat Mass Transf.* 111:532–39
- Masuk A, Salibindla A, Ni R. 2021. Simultaneous measurements of deforming Hinze-scale bubbles with surrounding turbulence. *J. Fluid Mech.* 910:A21
- Maxey M. 2017. Simulation methods for particulate flows and concentrated suspensions. *Annu. Rev. Fluid Mech.* 49:171–93
- Mercader C, Lucas A, Derré A, Zakri C, Moisan S, et al. 2010. Kinetics of fiber solidification. *PNAS* 107(43):18331–35
- Monti A, Olivieri S, Rosti ME. 2023. Collective dynamics of dense hairy surfaces in turbulent flow. *Sci. Rep.* 13(1):5184
- Moosaie A, Manhart M. 2013. Direct Monte Carlo simulation of turbulent drag reduction by rigid fibers in a channel flow. *Acta Mech.* 224:2385–413
- Nunes J, Sadlej K, Tama J, Stone H. 2012. Control of the length of microfibers. *Lab Chip* 12(13):2301–4
- Oehmke T, Bordoloi A, Variano E, Verhille G. 2021. Spinning and tumbling of long fibers in isotropic turbulence. *Phys. Rev. Fluids* 6:044610
- Olivieri S, Brandt L, Rosti ME, Mazzino A. 2020. Dispersed fibers change the classical energy budget of turbulence via nonlocal transfer. *Phys. Rev. Lett.* 125(11):114501

- Olivieri S, Cannon I, Rosti ME. 2022a. The effect of particle anisotropy on the modulation of turbulent flows. *J. Fluid Mech.* 950:R2
- Olivieri S, Mazzino A, Rosti ME. 2021. Universal flapping states of elastic fibers in modulated turbulence. *Phys. Fluids* 33:071704
- Olivieri S, Mazzino A, Rosti ME. 2022b. On the fully coupled dynamics of flexible fibres dispersed in modulated turbulence. *J. Fluid Mech.* 946:A34
- Parrella F, Brizzolara S, Holzner M, Mitrano D. 2024. Impact of heteroaggregation between microplastics and algae on particle vertical transport. *Nat. Water* 2:541–52
- Paschkewitz J, Dimitropoulos C, Hou Y, Somandepalli V, Mungal M, et al. 2005. An experimental and numerical investigation of drag reduction in a turbulent boundary layer using a rigid rodlike polymer. *Phys. Fluids* 17:085101
- Paschkewitz J, Dubief Y, Dimitropoulos C, Shaqfeh E, Moin P. 2004. Numerical simulation of turbulent drag reduction using rigid fibres. *J. Fluid Mech.* 518:281–317
- Pei Z, Zhang Y, Zhou J. 2018. A model for the particle-level simulation of multiple flexible fibers moving in a wall-bounded fluid flow. *J. Fluids Struct.* 80:37–58
- Peskin C. 1972. Flow patterns around heart valves: a numerical method. *J. Comput. Phys.* 10(2):252–71
- Picardo J, Singh R, Ray Samriddhi S, Vincenzi D. 2020. Dynamics of a long chain in turbulent flows: impact of vortices. *Philos. Trans. R. Soc. A* 378:20190405
- Picardo J, Vincenzi D, Pal N, Ray SS. 2018. Preferential sampling of elastic chains in turbulent flow. *Phys. Rev. Lett.* 121:244501
- Pinelli A, Naqavi I, Piomelli U, Favier J. 2010. Immersed-boundary methods for general finite-difference and finite-volume Navier–Stokes solvers. *J. Comput. Phys.* 229(24):9073–91
- Pope SB. 2001. *Turbulent Flows*. Cambridge University Press
- Powers T. 2010. Dynamics of filaments and membranes in a viscous fluid. *Rev. Mod. Phys.* 82(2):1607–31
- Pujara N, Du Clos K, Ayres S, Variano E, Karp-Boss L. 2021. Measurements of trajectories and spatial distributions of diatoms (*Coscinodiscus* spp.) at dissipation scales of turbulence. *Exp. Fluids* 62:149
- Rosti ME, Banaei A, Brandt L, Mazzino A. 2018. Flexible fiber reveals the two-point statistical properties of turbulence. *Phys. Rev. Lett.* 121:044501
- Rosti ME, Olivieri S, Banaei AA, Brandt L, Mazzino A. 2020. Flowing fibers as a proxy of turbulence statistics. *Meccanica* 55:357–70
- Shin M, Koch D. 2005. Rotational and translational dispersion of fibres in isotropic turbulent flows. *J. Fluid Mech.* 540:143–73
- Singh R, Gupta M, Picardo JR, Vincenzi D, Ray SS. 2020. Elastoinertial chains in a two-dimensional turbulent flow. *Phys. Rev. E* 101:053105
- Snook B, Guazzelli E, Butler J. 2012. Vorticity alignment of rigid fibers in an oscillatory shear flow: role of confinement. *Phys. Fluids* 24(12):121702
- Soldati A, Marchioli C. 2009. Physics and modelling of turbulent particle deposition and entrainment: review of a systematic study. *Int. J. Multiphase Flow* 35(9):827–39
- Sugathapala M, Capuano T, Brandt L, Iudicone D, Sardina G. 2025. Vertical transport of buoyant microplastic particles in the ocean: the role of turbulence and biofouling. *Environ. Pollut.* 369:125819
- Sulaiman M, Climent E, Delmotte B, Fede F, Plouraboué F, Verhille G. 2019. Numerical modelling of long flexible fibers in homogeneous isotropic turbulence. *Eur. Phys. J. E* 42:132
- Switzer L, Klingenberg D. 2004. Flocculation in simulations of sheared fiber suspensions. *Int. J. Multiphase Flow* 30:67–87
- Tang Y, Wu T-H, He G-W, Qi D. 2018. Multi-flexible fiber flows: a direct-forcing immersed boundary lattice-Boltzmann lattice-spring approach. *Int. J. Multiphase Flow* 99:408–22
- Tatsii D, Bucci S, Bhowmick T, Guettler J, Bakels L, et al. 2024. Shape matters: long-range transport of microplastic fibers in the atmosphere. *Environ. Sci. Technol.* 58:671–82
- Verhille G. 2022. Deformability of discs in turbulence. *J. Fluid Mech.* 933:A3
- Verhille G, Bartoli A. 2016. 3D conformation of a flexible fiber in a turbulent flow. *Exp. Fluids* 57:117
- Voth GA, Soldati A. 2017. Anisotropic particles in turbulence. *Annu. Rev. Fluid Mech.* 49:249–76
- White C, Mungal M. 2008. Mechanics and prediction of turbulent drag reduction with polymer additives. *Annu. Rev. Fluid Mech.* 40:235–56

- Wilkinson M, Mehlig B. 2005. Caustics in turbulent aerosols. *Europhys. Lett.* 71:186–92
- Wu J, Aidun C. 2010. A method for direct simulation of flexible fiber suspensions using lattice Boltzmann equation with external boundary force. *Int. J. Multiphase Flow* 36(3):202–9
- Xu D, Wang B, Yu Z, Guo Y. 2023. Clustering in gas-fluidized riser flows of flexible fibers. *AIChE J.* 69(4):e18024
- Yamakawa H. 1971. *Modern Theory of Polymer Solutions*. Harper & Row
- Yu Z. 2005. A DLM/FD method for fluid/flexible-body interactions. *J. Comput. Phys.* 207(1):1–27